FULL PAPER

Magnetic Resonance in Medicine 00:00–00 (2016)

Robustness of Spatio-Temporal Regularization in Perfusion MRI Deconvolution: An Application to Acute Ischemic Stroke

Mathilde Giacalone,[1] Carole Frindel,[1] Marc Robini,[1] Frédéric Cervenansky,[1] Emmanuel Grenier,[2] and David Rousseau[1]*

Purpose: The robustness of a recently introduced globally convergent deconvolution algorithm with temporal and edge-preserving spatial regularization for the deconvolution of dynamic susceptibility contrast perfusion magnetic resonance imaging is assessed in the context of ischemic stroke.

Theory and Methods: Ischemic tissues are not randomly distributed in the brain but form a spatially organized entity. The addition of a spatial regularization term allows to take into account this spatial organization contrarily to the sole temporal regularization approach which processes each voxel independently. The robustness of the spatial regularization in relation to shape variability, hemodynamic variability in tissues, noise in the magnetic resonance imaging apparatus, and uncertainty on the arterial input function selected for the deconvolution is addressed via an original in silico validation approach.

Results: The deconvolution algorithm proved robust to the different sources of variability, outperforming temporal Tikhonov regularization in most realistic conditions considered. The limiting factor is the proper estimation of the arterial input function.

Conclusion: This study quantified the robustness of a spatio-temporal approach for dynamic susceptibility contrast-magnetic resonance imaging deconvolution via a new simulator. This simulator, now accessible online, is of wide applicability for the validation of any deconvolution algorithm. **Magn Reson Med 000:000–000, 2016. © 2016 International Society for Magnetic Resonance in Medicine.**

Key words: deconvolution; digital phantoms; dynamic susceptibility contrast perfusion MRI; stroke

INTRODUCTION

Dynamic susceptibility contrast (DSC) perfusion magnetic resonance imaging (MRI) is an imaging modality, mainly used in clinical routine for the evaluation of cerebral perfusion in stroke or brain cancer patients (1). In the context of acute ischemic stroke, perfusion imaging allows the estimation of hemodynamic parameters in the brain and is used in diagnosis and patient management. Its application is, for example, the evaluation of the tissue at risk of infarction or the assessment of the risk of intracranial hemorrhage. Although largely disseminated in clinic and clinical research for acute stroke, the quantitative benefit of the use of DSC perfusion MRI is still discussed because many issues remain to be overcome (2) in the processing of the images. Among them, we will focus here on the issue of data deconvolution.

Deconvolution is used in DSC-MRI analysis to assess the hemodynamic parameters of clinical interest: it computes a three dimensional and temporal ($3D + t$) image where each voxel is associated to a temporal signal from which the hemodynamic parameters can be extracted. This step corresponds to the resolution of an ill-posed inverse problem. Consequently, in order to obtain a stable solution, additional prior information on the desired solution needs to be used. Generally, prior information enforces a constraint on the solution whose strength is determined by a regularization parameter. Most deconvolution approaches consider each voxel independently—imposing constraints in the temporal dimension only—and ignore the spatial correlation between neighboring voxels that is inherent to the structured organization of the brain tissue. A common approach consists in adding a temporal regularization constraint which imposes a certain smoothness over time. With such a deconvolution approach, the hemodynamic parameter maps extracted after deconvolution often contain isolated voxels with abberant values. To address this problem, deconvolution approaches with spatial and temporal regularization constraints were recently introduced (3–7).

The deconvolution algorithm proposed by Frindel et al. (6) contains an edge-preserving spatial regularization constraint and has the added advantage of being globally convergent, which ensures that the algorithm systematically provides optimum performance and does not run the risk of being stuck in a local minimum. This robustness is very important in the context of clinical image analysis where fluctuations of a tool's performance cannot be accepted. In this original paper, the algorithm was tested on synthetic and real data for large compact ischemic lesions. The quality of the hemodynamic parameter maps obtained after deconvolution with the Frindel algorithm (6) was considerably improved compared with maps obtained after deconvolution with either the truncated singular value decomposition (8) or the Tikhonov regularization (9) methods, both methods which contain only a temporal regularization constraint. These results showed the benefit of taking into account the spatio-temporal nature of the data. However, studies (10–14) focusing on the ischemic lesion shapes and their potential interest in predicting the

[1]University of Lyon, INSA-Lyon, Université Claude Bernard Lyon 1, CNRS, Inserm, CREATIS UMR 5220, U1206, LYON, F69006, France.

[2]ENS-Lyon, UCB Lyon, Inria, NUMED, CNRS, UMPA UMR 5669, LYON, F69007, France

*Correspondence to: David Rousseau, PhD, CREATIS - INSA LYON (Direction), Bâtiment Blaise Pascal (4ème étage), 7 Avenue Jean, Capelle, 69621 Villeurbanne Cedex, France. E-mail: david.rousseau@creatis.insa-lyon.fr

Received 1 August 2016; revised 16 November 2016; accepted 16 November 2016

DOI 10.1002/mrm.26573

Published online 00 Month 2016 in Wiley Online Library (wileyonlinelibrary.com).

outcome of stroke, have brought to light the great variability of lesion shapes. They showed that in acute stroke, ischemic lesions do not necessarily present a compact shape but can have a fragmented aspect. Since the Frindel algorithm (6) imposes a spatial regularization constraint, it is possible that the optimum strength of the constraint, controlled by the value of its regularization parameter, will differ for compact and fragmented tissue organizations. In the context of clinical image analysis however, it is crucial that the deconvolution algorithm always gives results of good quality in spite of individual patient biodiversity.

Given the promising results obtained with the Frindel algorithm (6) on compact lesions, we propose to assess here the performance and robustness of the algorithm when confronted with lesion shape variability. Since lesion shape variability is not the sole possible source of variability, we will compare its relative impact on the performance of the deconvolution algorithm with other sources of variability. First, we will look at the impact of hemodynamic tissue variability. Then, since the signal to noise ratio is rather small in DSC-MRI due to the necessity of a fast MRI sequence in patient management in the acute phase, we will look at the impact of noise in the MRI acquisition system. Finally, the deconvolution process requires an estimate of the arterial input function and we will therefore look at the impact of errors on the estimation. We propose to address this issue via an original in silico validation approach with realistic lesion shapes.

THEORY

Principles of Perfusion DSC-MRI Deconvolution

A DSC-MRI perfusion image consists of a time series of T_2- or T_2^*- weighted MRI images, the acquisitions of which are synchronized with the injection of a contrast-agent. The contrast-agent tissular concentration over time in each voxel is estimated from the perfusion image. For each voxel, the profile of the contrast-agent concentration signal gives insight into the state of the micro-circulation in the tissues within the voxel and can be used to estimate regional hemodynamic parameters of clinical interest, such as the cerebral blood flow (CBF) or the mean transit time. The profiles of the contrast-agent concentration signals also depend on the volume and dispersion of the so-called arterial input function (AIF), which corresponds to the profile of the contrast-agent bolus upon its arrival in the brain tissue. Based on the indicator-dilution theory (15), the contrast-agent concentration signal in voxel v, $C_v(t)$ (mM), can be modeled by the convolution of the AIF, $C_a(t)$ (mM), and the tissue impulse response function, $f_v(t)$ (mL. g^{-1}. s^{-1}), which contains the hemodynamic information of interest:

$$C_v(t) = \kappa . \int_0^t C_a(\tau) f_v(t-\tau) d\tau \text{ with } f_v(t) = \mathrm{CBF}_v \times R_v(t, \mathrm{MTT}_v), \quad [1]$$

where κ (g. mL^{-1}) depends on the brain tissue density and on the hematocrit level in the capillaries and arterioles. Generally, its value cannot be measured and it is common practice to suppose it constant (e.g., $\kappa = 1$ g. mL^{-1}). CBF_v (mL. g^{-1}. s^{-1}) corresponds to the cerebral blood flow in voxel v. $R_v(t)$ (no unit) is the residue function in voxel v. It describes the fraction of contrast-agent still present in voxel v at time t (s). MTT_v (s) corresponds to the mean transit time in voxel v.

In order to eliminate the variability due to the AIF, the deconvolution of the contrast-agent concentration image by the AIF needs to be carried out (16). It consists in computing the tissue impulse response function image $\boldsymbol{f}$ from the contrast-agent concentration image $\boldsymbol{C}$ and the arterial input function C_a.

Deconvolution Algorithm

The Frindel algorithm (6) addresses the deconvolution problem as the minimization, over the impulse response function image $\boldsymbol{f}$, of a global cost function $\Omega(\boldsymbol{f})$ composed of a data-fidelity term $\Phi(\boldsymbol{f})$, a temporal regularization constraint $\Psi_t(\boldsymbol{f})$, and an edge-preserving spatial regularization constraint $\Psi_s(\boldsymbol{f})$:

$$\Omega(\boldsymbol{f}) = \Phi(\boldsymbol{f}) + \lambda_t \Psi_t(\boldsymbol{f}) + \lambda_s \Psi_s(\boldsymbol{f}, \delta), \quad [2]$$

where λ_t, λ_s, and δ are the parameters of the algorithm. In this cost function, the data fidelity term penalizes deviations from the observed data, the temporal regularization term penalizes solutions which are not smooth as a function of time (i.e., with a large temporal gradient norm) and the edge-preserving spatial regularization term favors solutions which are smooth spatially (i.e., with a small spatial gradient norm) but which still preserve the main spatial discontinuities in the image. The temporal regularization term is the well-known Tikhonov regularization (9) and is expressed as $\Psi_t(\boldsymbol{f}) = ||\mathrm{T}\boldsymbol{f}||_2^2$ where T corresponds to a first-order difference operator. More details on the cost function terms can be found in (6) and (7).

The regularization parameters, λ_t and λ_s, control the strength of the temporal and edge-preserving spatial regularization terms with respect to the data fidelity term, while the scaling parameter, δ, controls the value of the spatial gradient above which edges should be preserved by the algorithm. Parameters λ_t, λ_s, and δ need to be selected to optimize the performance of the algorithm. An automatized and unsupervized solution to select these parameters was proposed recently (17). In this study, we address the question of the robustness of the algorithm of Equation [2] when we depart, due to various sources of variability, from the original set-up for which the parameters were optimized.

METHODS

In order to evaluate the performance and robustness of the Frindel deconvolution algorithm (6), we decided to adopt a numerical simulation approach since it enables a fine control of all the sources of variability, notably, as stressed in the introduction, lesion shape variability. To the best of our knowledge, none of the simulators available in the literature included realistic ischemic lesion shapes. Consequently, we developed a new simulator for the validation of deconvolution algorithms for DSC-MRI

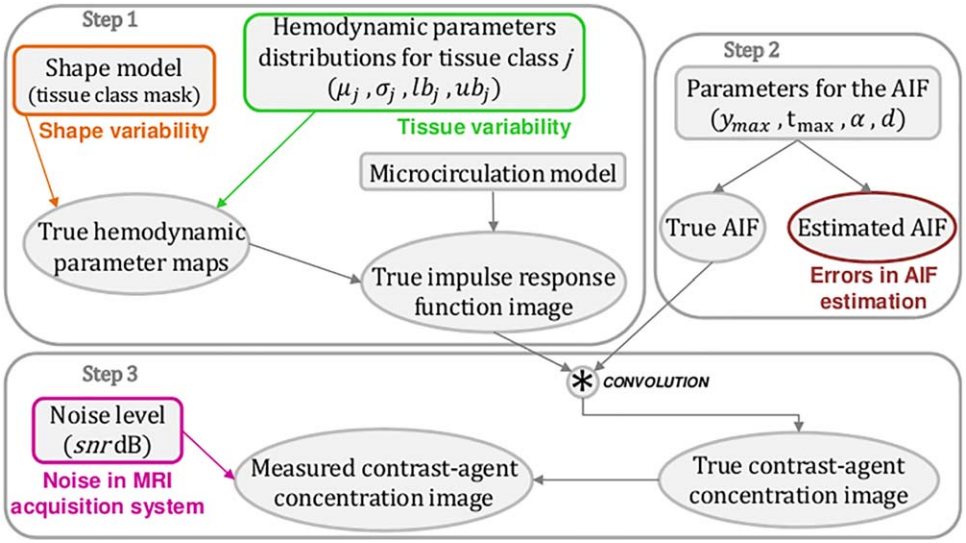

FIG. 1. Pipeline for the DSC-MRI concentration image simulator.

which uses the widespread simulation approach consisting of simulating directly the contrast-agent concentration images using the principle of the indicator-dilution theory formulated in Equation [1]. We then made full use of the simulator in order to test the robustness of the Frindel deconvolution algorithm (6). Please note that the simulator as well as an implementation of this algorithm was made accessible online via the Virtual Imaging Platform at www.creatis.insa-lyon.fr/vip (18) (see Supporting Information for a tutorial on the use of the online simulator).

Numerical Simulator for the Validation of Deconvolution Algorithms

Kudo et al. (19) proposed a digital phantom for the study of the precision and reliability of perfusion DSC-MRI analysis softwares. However, although their simulations are extremely valuable for the evaluation of deconvolution algorithms with temporal regularization constraints, they do not take into account any shape aspect. The only digital phantoms in the literature with realistic shapes were proposed for different imaging modality, such as CT brain perfusion (20) or DCE-MRI (21). Amongst the different articles on deconvolution algorithms with spatio-temporal regularization constraints, Schmid et al. (3) only used real patient data for the validation of their algorithm, He et al. (4) and Frindel et al. (6) used some synthetic data with simple and compact geometric shapes, and Schmid (5) used some synthetic data with geometric concentric shapes mimicking the myocardial segments. In the end, to the best of our knowledge, no simulations in DSC-MRI of brain contrast-agent concentration images with realistic shapes and applied to stroke pathology can be found in the literature. Also, when synthetic data were used to test the deconvolution algorithm of (6), piece-wise continuous tissues were considered and no tissue variability was introduced. This perfectly matched the spatial prior behind the edge-preserving spatial regularization. However, there is in reality some hemodynamic tissue variability and it can alter the performance of deconvolution algorithms with spatio-temporal regularization compared with the ideal case of a piece-wise continuous image.

We, therefore, modified the simulator of (19) to propose a new simulator which allows the production of digital phantoms with realistic brain and lesion shapes, distinct classes of tissues and distinct realistic hemodynamic tissue distributions as well as simulates errors on the AIF. The complete simulation pipeline, illustrated in Figure 1, is described below.

Step 1—Simulation of the Impulse Response Function Image

We generate a $2D+t$ (or $3D+t$) impulse response function image from a two-dimensional (2D) (or three-dimensional (3D)) label mask representing the spatial distribution of the different classes of tissues. The label mask, which will be refered to as "shape model" from now on, is an input of the simulator. Its choice is very important since it determines the degree of realism of the simulation in terms of number of tissue classes and spatial organization.

Each voxel v in the 2D (or 3D) spatial domain is associated to a one-dimensional signal $f_v(t)$ representing the impulse response function of this voxel. Different models representing potential shapes for the tissue impulse response function have been proposed in the literature (8,9,22). In our simulator, the choice between a box-shaped, triangular or single exponential first-order model is given:

$$[f_v(t)]_{\text{box-shaped}} = \begin{cases} \text{CBF}_v & \text{if } t \leq \text{MTT}_v \\ 0 & \text{if } t > \text{MTT}_v \end{cases}, \quad [3]$$

$$[f_v(t)]_{\text{triangular}} = \begin{cases} \text{CBF}_v.\left(1 - \dfrac{t}{2.\text{MTT}_v}\right) & \text{if } t \leq 2.\text{MTT}_v \\ 0 & \text{if } t > 2.\text{MTT}_v \end{cases}, \quad [4]$$

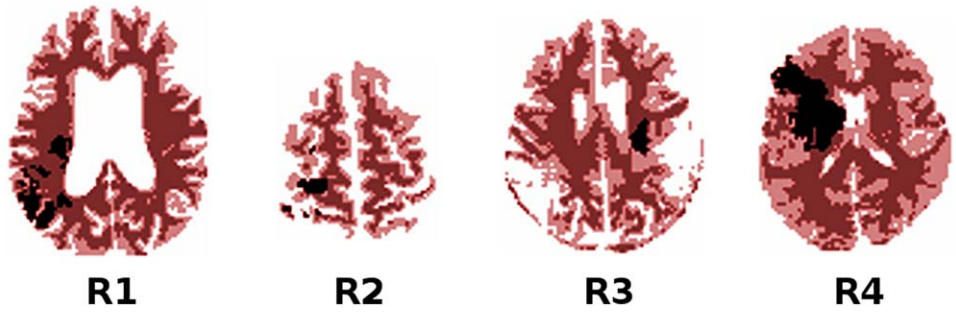

FIG. 2. Shape models chosen for this study. In dark red, the healthy white matter; in light red, the healthy gray matter; in black, the ischemic tissues.

$$[f_v(t)]_{\text{exponential}} = \text{CBF}_v.\exp\left(-\frac{t}{\text{MTT}_v}\right). \quad [5]$$

The values of the hemodynamic parameters CBF_v and MTT_v are drawn from a distribution specific to the tissue class associated to the voxel v by the shape model. In our simulator, we model independently the CBF and the mean transit time distributions as truncated Gaussian distributions. We therefore need four parameters: the mean μ, the standard deviation σ, the lower bound lb and the upper bound ub. The values of these parameters (μ, σ, lb, ub) for both the CBF and the mean transit time and for each tissue class is an input of the simulator and determine the level of intraclass tissue variability and interclass tissue separability.

Step 2—Simulation of the Arterial Input Function

A global arterial input function $C_a(t)$ is generated. $C_a(t)$ is modeled by a gamma-variate function, expressed with the formulation proposed by Madsen (23):

$$C_a(t) = \begin{cases} 0 & \text{si } t \leq d \\ y_{\max}.(\frac{t-d}{t_{\max}})^{\alpha}.\exp\left(\alpha(1-\frac{t-d}{t_{\max}})\right) & \text{si } t > d \end{cases}, \quad [6]$$

where $y_{\max}$ and $t_{\max}$ correspond respectively to the magnitude and the location of the AIF maximum, d is the tracer arrival time and α the shape parameter of the AIF. $(y_{\max}, t_{\max}, d, \alpha)$ are input parameters of the simulator.

Also, a flawed version of the global arterial input function is generated in order to evaluate the impact of errors in the AIF estimation on the performance of the deconvolution. In the literature, several studies examined the effect of specific AIF estimation errors on the quantification of DSC-MRI (24–27) but, to the best of our knowledge, none gave a statistical model for the errors on the AIF estimation in their specific framework of study. Meijs et al. (28) recently proposed a bivariate Gaussian model on the $y_{\max}$ and $t_{\max}$ to describe the inter-patient variability in the arterial input function. Similar to the work of Calamante and Connelly (25), we propose here to model AIF estimation errors as perturbations on the $y_{\max}$ and $t_{\max}$ of the arterial input function and sample the distorted values of $y_{\max}$ and $t_{\max}$ within the 95% confidence ellipse of the model of Meijs et al. (28) rescaled to and centered around the true $y_{\max}$ and $t_{\max}$ values. These values serve as an upper bound for the intrapatient estimation errors on the AIF.

Step 3—Simulation of the Contrast-Agent Concentration Image

The contrast-agent concentration image is generated using Equation [1]. Each noise free concentration time curve $C_v(t)$ is simulated by convolving the arterial input function $C_a(t)$ of step 2 with the tissue impulse response function $f_v(t)$ of step 1. For the convolution, a trapezoidal method is used to approximate the integral and, in order to reduce discretization artifacts, $C_a(t)$ and $f_v(t)$ are discretized with a sampling rate 10 times higher than dt, the target temporal resolution of $C_v(t)$. The signals are then under-sampled to achieve the temporal resolution dt. We have $t \in [0{:}T]$, with T the duration of the MRI acquisition. Finally, a realistic noise is added to the noise free concentration image by following the procedure proposed by Smith et al. (29). Each noise free concentration time curve $C_v(t)$ is transferred into the signal intensity domain giving $S_v(t) = S_0 \exp\left(-k_{R_2^*}.\text{TE}.C_v(t)\right)$, where the baseline value S_0 is 200 a.u., the echo time TE is $50 * 10^{-3}$ s and the proportionality constant $k_{R_2^*}$ is determined such that the mean concentration time curve in the brain tissue achieves a 40% peak signal decrease in the signal intensity domain (19). A Gaussian noise of mean zero and standard deviation $\sigma_{\mathcal{N}}$ is added to the noise free signal intensity image to simulate noise in the MRI acquisition system. The standard deviation value $\sigma_{\mathcal{N}}$ is computed in order to obtain a signal to noise ratio of snr, where the SNR is defined in decibel as $20\log_{10}(S_0/\sigma_{\mathcal{N}})$. The noisy concentration image is then recovered with the inverse transform $[C_v(t)]_{\text{noisy}} = -\frac{1}{k_{R_2^*}.\text{TE}} \ln\left(\frac{[S_v(t)]_{\text{noisy}}}{S_0}\right)$. ($dt$,$T$, snr) are input parameters of the simulator.

Robustness Analysis

Dataset Simulation for the Robustness Analysis

We test the robustness of the deconvolution algorithm to shape variability and evaluate its impact on the performance of the algorithm in comparison with other sources of variability (i.e., tissue variability, noise in the MRI acquisition system, or errors in the arterial input function estimation). The impact of a given source of variability is studied while the other sources are kept constant.

In order to simulate shape variability, we need to use shape models representative of the shape variability observed on clinical data. We studied the european I-

Table 1
Optimum set of Regularization Parameters $\Lambda_{R_i} = (\lambda_t, \lambda_s)$ Selected for Shape Model R_i in the (ST) and (T) Contexts of the Frindel Algorithm (6)

	Λ_{R_1}	Λ_{R_2}	Λ_{R_3}	Λ_{R_4}
(ST)	(3.65, 0.422) $\times 10^{-2}$	(3.65, 0.649) $\times 10^{-2}$	(3.16, 0.750) $\times 10^{-2}$	(1.00, 0.0750) $\times 10^{-2}$
(T)	(7.50,0) $\times 10^{-3}$	(5.62,0) $\times 10^{-3}$	(4.87,0) $\times 10^{-3}$	(7.50,0) $\times 10^{-3}$

KNOW database (14) and constructed, from real patient images, four shape models (R_1, R_2, R_3, and R_4) with ischemic lesion shapes and tissue distributions representative of the variability observed in the database (see Fig. 2). Shape model R1 represents a large-sized fragmented lesion, shape model R2 represents a medium-sized fragmented lesion, shape model R3 represents a small-sized compact lesion and shape model R4 represents a large-sized compact lesion. These shape models were selected via an unsupervised clustering of the acute DWI lesion shapes in the I-KNOW database (see Supporting Information for more details). We chose to consider three classes of tissues: healthy white matter, healthy gray matter and core ischemic lesion. Information in the literature concerning intrapatient and intraclass tissue variability is relatively scarce. Moreover, the hemodynamic parameters are age-dependent and vary, for the ischemic lesion, with the severity of the stroke and the region under consideration (DWI lesion, mismatch, penumbra...). Combining different information found in the literature (16,30–34) we chose the following simulation parameters. For healthy gray tissue, healthy white tissue and ischemic tissue, respectively: $\mu_{CBF} = (60,\ 25,\ 10)$, $\sigma_{CBF} = (9,\ 2.1,\ 4.3)$, $lb_{CBF} = (0,\ 0,\ 0)$ and $ub_{CBF} = (200,\ 200,\ 200)$ mL/100 g/min; $\mu_{MTT} = (4,\ 4.8,\ 10)$, $\sigma_{MTT} = (2.2,\ 3.2,\ 5)$, $lb_{MTT} = (0,\ 0,\ 0)$ and $ub_{MTT} = (25,\ 25,\ 25)$ s. For background voxels, we simply set $C_v(t) = 0$ at all time t. In order to simulate noise in the MRI acquisition system, we chose a SNR of 40 dB, a value found in the perfusion images of the I-KNOW database. Finally, we use an exponential model for the impulse response function and, based on information found in the literature (8,34,35), we set the other input parameters to the following values: y_{max}=0.6124 mM, t_{max}=4.5 s, d=3 s, α=3, $dt = 1$ s, $T = 56$ s.

Performance Evaluation

The performance of the deconvolution algorithm is assessed with two quality criteria, the mean absolute error on the CBF and the root mean square error on the impulse response function. For these two criteria, the smaller the value, the better the quality of the deconvolved image. The mean absolute error compares the CBF map estimated after deconvolution ($\widehat{\mathbf{CBF}}$) to the expected CBF map (**CBF**):

$$\mathrm{MAE} = \frac{1}{N_v} \sum_{v \in \mathrm{brain}} |\widehat{\mathrm{CBF}}_v - \mathrm{CBF}_v| \,. \qquad [7]$$

The root mean square error, contrarily to the mean absolute error, is an overall quality criteria and compares the entire impulse response image obtained after deconvolution ($\hat{\mathbf{f}}$) to the expected impulse response image ($\boldsymbol{f}$):

Table 2
Performance (Mean ± SD) of the Frindel Algorithm (6) for the Deconvolution, with the True AIF, of $n = 6$ Contrast-Agent Concentration Images Simulated with Each Shape Model R_i When We Use for the Deconvolution the Optimum Set of Regularization Parameters Λ_{R_i} or When We Use Another Set of Regularization Parameters Λ_{R_j}, with $j \neq i$

			Parameters used for deconvolution			
Shape model			Λ_{R_1}	Λ_{R_2}	Λ_{R_3}	Λ_{R_4}
NMAE (%)	(ST)	R_1	7.68 ± 0.05	8.26 ± 0.08	8.61 ± 0.08	7.99 ± 0.06
		R_2	9.48 ± 0.26	9.15 ± 0.31	9.28 ± 0.30	9.81 ± 0.30
		R_3	9.23 ± 0.17	8.41 ± 0.20	8.29 ± 0.20	9.20 ± 0.20
		R_4	9.23 ± 0.15	9.27 ± 0.13	8.99 ± 0.12	8.26 ± 0.04
	(T)	R_1	9.25 ± 0.12	9.30 ± 0.11	9.34 ± 0.10	9.25 ± 0.12
		R_2	11.05 ± 0.27	10.96 ± 0.28	10.97 ± 0.27	11.05 ± 0.27
		R_3	10.54 ± 0.25	10.51 ± 0.25	10.48 ± 0.25	10.54 ± 0.25
		R_4	9.85 ± 0.12	9.92 ± 0.12	9.94 ± 0.12	9.85 ± 0.12
NRMSE (%)	(ST)	R_1	5.78 ± 0.02	6.14 ± 0.02	6.39 ± 0.02	5.19 ± 0.03
		R_2	6.83 ± 0.02	7.38 ± 0.02	7.64 ± 0.02	5.96 ± 0.04
		R_3	6.26 ± 0.04	6.75 ± 0.03	6.85 ± 0.04	5.55 ± 0.04
		R_4	5.12 ± 0.02	5.54 ± 0.02	5.80 ± 0.02	4.70 ± 0.02
	(T)	R_1	8.08 ± 0.05	8.89 ± 0.05	9.17 ± 0.05	8.08 ± 0.05
		R_2	9.33 ± 0.11	10.33 ± 0.15	10.90 ± 0.17	9.33 ± 0.11
		R_3	9.03 ± 0.03	9.94 ± 0.04	10.49 ± 0.04	9.03 ± 0.03
		R_4	8.12 ± 0.02	9.13 ± 0.03	9.44 ± 0.03	8.12 ± 0.02

For each shape model, the worst result obtained in the (ST) context between the four set of regularization parameters is systematically better than the best result obtained in the (T) context. This is illustrated in gray for patient R_1 and quality criteria NMAE.

Table 3
Quantification of the Impact of Tissue Variability—Performance (Mean ± SD) of the Frindel Algorithm (6) for the Deconvolution, with the True AIF, of $n = 30$ Contrast-Agent Concentration Images Simulated from Each Shape Model R_i

	NMAE (%)			NRMSE (%)		
Shape Model	(T)	(ST)	(T)-(ST)	(T)	(ST)	(T)-(ST)
R1	9.08 ± 0.17	7.53 ± 0.22	1.55 ± 0.17***	7.70 ± 0.07	5.77 ± 0.03	1.92 ± 0.06***
R2	11.07 ± 0.24	9.07 ± 0.24	2.00 ± 0.16***	10.06 ± 0.11	7.36 ± 0.04	2.70 ± 0.10***
R3	10.38 ± 0.21	8.21 ± 0.22	2.17 ± 0.15***	10.27 ± 0.06	6.85 ± 0.03	3.42 ± 0.06***
R4	9.76 ± 0.15	8.17 ± 0.13	1.59 ± 0.13***	7.9 ± 0.04	4.77 ± 0.03	3.13 ± 0.04***

The contrast-agent concentration images are simulated by generating a new realization of the hemodynamic maps every time (see Figure 1, green frame in step 1) while keeping everything else in the simulation pipeline strictly identical. Significance codes for the paired *t*-tests: *** for *P*-value ≤0.001, else ** for *P*-value ≤0.01, else * for *P*-value ≤0.05, else • for *P*-value ≤0.1, else † for *P*-value ≤1.

$$\mathrm{RMSE} = \sqrt{\frac{1}{N_t N_v} \sum_{v \in \mathrm{brain}} \sum_{i=1}^{N_t} \left(\widehat{f_v}(t_i) - f_v(t_i) \right)^2}. \qquad [8]$$

For easier interpretation of these quality criteria values, we will normalize these two quality criteria by the mean CBF in the healthy gray matter to obtain NMAE and NRMSE (here $\mu_{\mathrm{CBF}_{\mathrm{healthy+gray}}} = 60$ mL/100 g/min).

Since using a temporal regularization constraint only is still the reference for data deconvolution in clinical applications, we look at the performance of the deconvolution algorithm in both the spatio-temporal regularization context (ST) and the temporal regularization context only (T). The temporal regularization context is accessible with the algorithm of Equation [2] by fixing $\lambda_s = 0$ and corresponds to the well-known Tikhonov regularization (9). The deconvolution algorithm in the (T) context is a pure voxel by voxel temporal regularization approach, meaning that the fluctuations in its performance are not due to shape variability but to noise. Therefore, we want to know how results obtained with the deconvolution algorithm in the (ST) context (6) compare with results obtained with the algorithm in the (T) context. The deconvolution algorithm with the spatio-temporal regularization will be considered robust to a source of variability if its performance, as measured by the NMAE and NRMSE, stays better than the performance in the purely (T) context. In order to compare the performance in the (ST) and (T) contexts, we use a paired *t*-test, the null hypothesis being that the true mean difference between the performance in the two contexts is zero.

Implementation and Optimization of the Deconvolution Algorithm

The deconvolution algorithm proposed in (6) was implemented and a preliminary step of normalization of the data by the maximum value of the AIF was added to the deconvolution pipeline. This step allows the use, for all images, of a fixed value for the scaling parameter δ which controls the value of the spatial gradient above which edges should be preserved by the deconvolution algorithm (data not shown). After empirical testing, we set $\delta = 10^{-7}$.

Here, we simulated six contrast-agent concentration images for each shape model R_i, and deconvolved them (with the true AIF) for a very wide range of regularization parameters $\Lambda = (\lambda_t, \lambda_s)$. The optimum set of regularization parameters for each shape model R_i, Λ_{R_i}, is then set, once and for all, as the set of regularization parameters minimizing the average NMAE after deconvolution over the six images.

RESULTS

Robustness to Shape Variability

Table 1 shows the regularization parameters that were selected for the different shape models. The comparative performance of the deconvolution algorithm in the (ST) and (T) contexts is given in Table 2. The average performance in the (ST) context (8.34% for the NMAE and 6.18% for the NRMSE, all shape models confounded) is systematically better than in the (T) context (10.13% for the NMAE and 9.25% for the NRMSE, all shape models confounded). Moreover, the worst result obtained in the

Table 4
Quantification of the Impact of Noise in the MRI Acquisition System—Performance (Mean ± SD) of the Frindel Algorithm (6) for the Deconvolution, with the True AIF, of $n = 30$ Contrast-Agent Concentration Images Simulated from Each Shape Model R_i

	NMAE (%)			NRMSE (%)		
Shape Model	(T)	(ST)	(T)-(ST)	(T)	(ST)	(T)-(ST)
R1	9.33 ± 0.09	7.77 ± 0.05	1.56 ± 0.11***	7.59 ± 0.04	5.81 ± 0.01	1.78 ± 0.04***
R2	11.17 ± 0.14	9.56 ± 0.06	1.61 ± 0.14***	9.93 ± 0.06	7.38 ± 0.02	2.55 ± 0.05***
R3	10.25 ± 0.10	8.15 ± 0.04	2.11 ± 0.10***	10.34 ± 0.03	6.83 ± 0.01	3.52 ± 0.03***
R4	9.29 ± 0.09	7.88 ± 0.06	1.41 ± 0.10***	7.93 ± 0.03	4.70 ± 0.03	3.23 ± 0.03***

The contrast-agent concentration images are simulated by generating a new realization of the noise in the MRI acquisition system (see Figure 1, magenta frame in step 3) while keeping everything else in the simulation pipeline strictly identical. Significance codes for the paired *t*-tests: *** for *P*-value ≤ 0.001, else ** for *P*-value ≤ 0.01, else * for *P*-value ≤ 0.05, else \bullet for *P*-value ≤ 0.1, else † for *P*-value ≤ 1

Table 5
Quantification of the Impact of Errors in the Estimation of the AIF—Performance (Mean ± SD) of the Frindel Algorithm (6) for the Deconvolution of One Contrast-Agent Concentration Image Simulated from Each Shape Model R_i with $n = 30$ Different Flawed AIF, where Perturbations are Introduced on Both y_{max} and t_{max}

Shape Model	NMAE (%)			NRMSE (%)		
	(T)	(ST)	(T)-(ST)	(T)	(ST)	(T)-(ST)
R1	30.92 ± 26.43	31.37 ± 24.33	−0.45 ± 3.72 †	11.39 ± 4.25	8.90 ± 3.16	2.50 ± 1.41***
R2	25.26 ± 12.61	26.76 ± 12.42	−1.51 ± 3.10*	11.56 ± 2.08	9.24 ± 1.54	2.32 ± 1.21***
R3	31.36 ± 23.65	34.20 ± 22.75	−2.84 ± 3.26***	12.94 ± 3.67	9.78 ± 2.78	3.16 ± 1.59***
R4	25.99 ± 20.26	25.68 ± 20.05	0.31 ± 1.68 †	10.72 ± 3.29	8.17 ± 3.04	2.54 ± 0.90***

Significance codes for the paired *t*-tests: *** for *P*-value ≤ 0.001, else ** for *P*-value ≤ 0.01, else * for *P*-value ≤ 0.05, else • for *P*-value ≤ 0.1, else † for *P*-value ≤ 1.

(ST) context is always better than the best result obtained in the (T) context.

This demonstrates the robustness of the deconvolution algorithm with spatio-temporal regularization (6) when confronted to a shape variability representative of the diversity found in ischemic lesions.

Robustness to Tissue Variability

Table 3 shows the performance of the deconvolution algorithm when confronted to tissue variability. The average performance in the (ST) context (8.24% for the NMAE and 6.19% for the NRMSE, all shape models confounded) is significantly better than in the (T) context (10.07% for the NMAE and 8.98% for the NRMSE, all shape models confounded). The variability in the performance is of the same order of magnitude in the (ST) and (T) contexts (0.20% vs. 0.19% for the NMAE and 0.03% vs. 0.07% for the NRMSE, all shape models confounded).

This demonstrates that, even when a realistic tissue variability is introduced and the image departs from the ideally piece-wise continuous image, there is a significant added value of the spatial regularization constraint. The deconvolution algorithm with spatio-temporal regularization (6) is, therefore, robust to tissue variability.

Robustness to Noise in the MRI Acquisition System

Table 4 shows the performance of the deconvolution algorithm when confronted to noise in the MRI acquisition system. The average performance in the (ST) context (8.34% for the NMAE and 6.18% for the NRMSE, all shape models confounded) is significantly better than in the (T) context (10.01% for the NMAE and 8.95% for the NRMSE, all shape models confounded). The variability in the performance is of the same order of magnitude in the (ST) and (T) contexts (0.05% vs. 0.10% for the NMAE and 0.02% vs. 0.04% for the NRMSE, all shape models confounded).

This demonstrates that the deconvolution algorithm with spatio-temporal regularization (6) is robust to a MRI acquisition noise at a signal-to-noise ratio level typical of clinical stroke data.

Robustness to Errors in the AIF Estimation

Table 5 shows the impact on the performance of the deconvolution algorithm of errors in the estimation of the magnitude (y_{max}) and position (t_{max}) of the maximum of the arterial input function. The impact of errors in the estimation of y_{max} and t_{max} are also evaluated separately in Tables 6 and 7, respectively, and illustrated on Figure 3. The impact of errors on the performance of the algorithm is more pronounced for the (ST) context than the (T) context. This means that the spatio-temporal approach is more sensitive to errors on the AIF than the temporal approach. The gain in using the spatial regularization constraint always stays significantly positive when considering the NRMSE, whereas in certain situations the gain vanishes or even becomes negative when considering the NMAE (e.g., Table 5, shape model R_3). This constitutes the limits of the robustness of the deconvolution algorithm with spatio-temporal regularization.

DISCUSSION

The deconvolution algorithm with spatio-temporal regularization proved robust when confronted with realistic shape variability, tissue variability or noise in the MRI acquisition system. The algorithm performed better in

Table 6
Quantification of the Impact of Errors in the Estimation of the AIF—Performance (Mean ± SD) of the Frindel Algorithm (6) for the Deconvolution of One Contrast-Agent Concentration Image Simulated from Each Shape Model R_i with $n = 30$ Different Flawed AIF, where Perturbations are Introduced on y_{max} Only

Shape Model	NMAE (%)			NRMSE (%)		
	(T)	(ST)	(T)-(ST)	(T)	(ST)	(T)-(ST)
R1	13.36 ± 4.33	13.72 ± 5.15	−0.36 ± 2.58 †	8.54 ± 1.51	6.46 ± 0.68	2.08 ± 1.12***
R2	15.46 ± 4.62	16.59 ± 6.13	−1.13 ± 3.03*	11.22 ± 1.94	8.02 ± 0.71	3.20 ± 1.45***
R3	14.88 ± 4.5	14.73 ± 5.91	0.15 ± 2.33 †	10.81 ± 1.84	7.41 ± 0.69	3.40 ± 1.45***
R4	14.91 ± 3.23	13.48 ± 2.85	1.43 ± 1.60***	8.45 ± 1.49	5.65 ± 0.65	2.80 ± 1.08***

Significance codes for the paired *t*-tests: *** for *P*-value ≤ 0.001, else ** for *P*-value ≤ 0.01, else * for *P*-value ≤ 0.05, else • for *P*-value ≤ 0.1, else † for *P*-value ≤ 1.

Table 7
Quantification of the Impact of Errors in the Estimation of the AIF—Performance (Mean ± SD) of the Frindel Algorithm (6) for the Deconvolution of One Contrast-Agent Concentration Image Simulated from Each Shape Model R_i with $n = 30$ Different Flawed AIF, where Perturbations are Introduced on t_{max} Only

Shape Model	NMAE (%)			NRMSE (%)		
	(T)	(ST)	(T)-(ST)	(T)	(ST)	(T)-(ST)
R1	16.20 ± 6.99	17.38 ± 7.68	−1.18 ± 1.97**	9.07 ± 1.14	7.21 ± 1.17	1.86 ± 0.13***
R2	16.51 ± 4.96	18.65 ± 5.84	−2.14 ± 2.24***	11.41 ± 1.44	8.92 ± 1.53	2.49 ± 0.13***
R3	21.62 ± 9.62	23.78 ± 9.60	−2.16 ± 1.88***	11.84 ± 1.15	8.68 ± 1.22	3.16 ± 0.14***
R4	16.58 ± 7.56	16.48 ± 7.49	0.11 ± 1.13 †	9.08 ± 1.12	6.35 ± 1.48	2.74 ± 0.43***

Significance codes for the paired *t*-tests: *** for *P*-value ≤ 0.001, else ** for *P*-value ≤ 0.01, else * for *P*-value ≤ 0.05, else • for *P*-value ≤ 0.1, else † for *P*-value ≤ 1.

the spatio-temporal regularization context than in the sole temporal regularization context when using Tikhonov regularization (9), and this when considering the quality of both the entire impulse response function image with the NRMSE or the CBF hemodynamic parameter map with the NMAE. This gain was obtained at the expense of a 100-fold increase of the computational time (4 min for the spatio-temporal approach vs. 3 s for the temporal approach for a $66 \times 77 \times 57$ 2D+t concentration image) with an implementation without parallelization on an Intel Core 7 CPU (2.10 GHz) computer.

The same robustness for the deconvolution algorithm was not found while investigating the impact of errors on the AIF estimation. The limiting factor of the performance of the deconvolution algorithm with spatio-temporal regularization appears to be errors on the AIF. The deconvolution algorithm is more sensitive to AIF errors in the spatio-temporal context than in the temporal regularization context. The performance of the algorithm in the spatio-temporal context is still systematically better than in the temporal context when considering the quality of the entire image after deconvolution (NRMSE), but, when considering only the quality of the CBF after deconvolution (NMAE), mixed results are obtained and the performance of the algorithm is not better in the spatio-temporal context than in the temporal context anymore.

This can in part be due to the fact that we used, as a model for the errors on the AIF, an existing interpatient

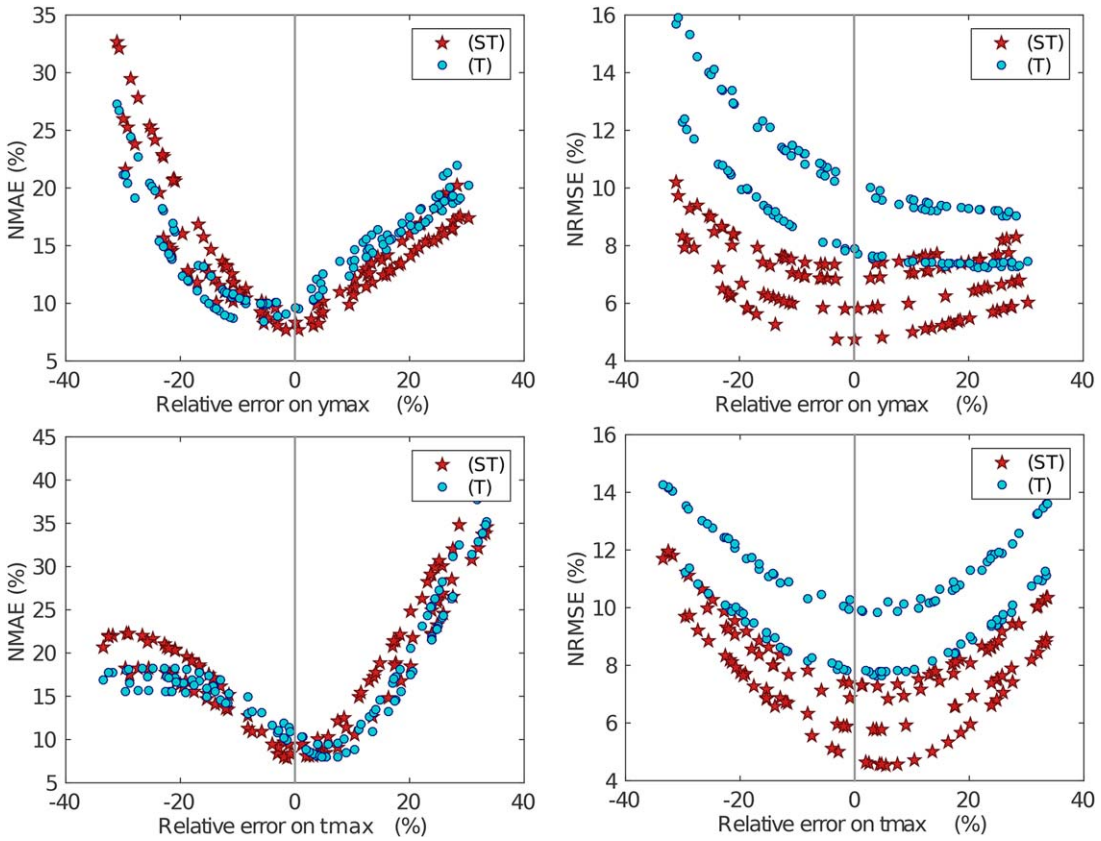

FIG. 3. Impact of errors in the estimation of y_{max} (top) or t_{max} (bottom) on the performance of the Frindel deconvolution algorithm (6), as quantified by the NMAE (left) or the NRMSE (right). In total, the results of the deconvolution of 120 simulations, 30 per shape model, are displayed here.

model of AIF variability (28) instead of an intrapatient AIF error model, which can result in an over estimation of the error. We believe it would be very useful in future research to develop a more precise statistical model for the estimation errors on the arterial input function in order to better quantify the limitations on the performance of the deconvolution algorithms due to these errors. These findings testify to the importance of working on methods for the AIF selection and also give rise to the question of whether one should use local arterial input functions rather than a global arterial input function for the deconvolution (24).

The simulation could be also enriched in other directions. Notably, it would be interesting to include, in addition to the core lesion tissue, other classes of tissues of biological significance in ischemic studies. Notably, it would be particularly interesting to complexify the ischemic tissue class to include both a "core lesion" region and a "tissue-at-risk" region, as well as to add a "large vessels" tissue class. Finally, it would be interesting to evaluate the effect of different types of artefacts on the performance of the deconvolution algorithms. For example, EPI-related artefact can cause spatial distortions in the vicinity of big vessels. However, such an improvement of the realism of the simulator would not be straightforward and another simulation approach consisting of simulating the whole MRI acquisition process using the Bloch equation would need to be used to simulate realistic EPI-related artefacts (26,36,37).

CONCLUSIONS

The first main contribution of this paper is the analysis, in the context of acute stroke, of the robustness of the deconvolution algorithm with spatio-temporal regularization proposed in (6). We used a new simulator to investigate the robustness of the deconvolution algorithm faced with different sources of variability encountered in the deconvolution of DSC-MRI acquired on acute stroke patients. The large variability of lesion shapes is found to have a negligible impact on the performance. The limiting factor for the performance of the algorithm is the proper estimation of the arterial input function. The recently introduced algorithm (6) outperformed deconvolution with a sole temporal Tikhonov regularization (9) in most realistic conditions tested with our numerical simulator. In the light of the recent proposition made in (17) for the unsupervised and automatic selection of the regularization parameters, these findings show that the deconvolution algorithm proposed in (6) is a promising solution.

The second main contribution of this paper is the introduction of a new numeric simulator for the validation of DSC-MRI perfusion deconvolution algorithms, notably those containing spatial regularization constraints. The simulator allows the robustness of deconvolution algorithms to be tested when faced with different sources of variability which can be encountered in DSC-MRI. It could be used for the benchmarking of any deconvolution algorithm, such as for example the truncated singular value decomposition deconvolution approach (8). The simulator is very flexible and allows the user an easy control over the degree of realism of the sources of variability. One should note that, although the present study was applied to acute stroke in human brain, the simulator in itself is generic and could be used for any DSC-MRI clinical application. Free online access to the simulator is given on the Virtual Imaging Platform (18) at www.creatis.insa-lyon.fr/vip.

ACKNOWLEDGMENTS

This work was performed within the framework of the LABEX PRIMES (ANR-11-LABX-0063) of Université de Lyon, within the program "Investissements d'Avenir" (ANR-11-IDEX-0007) operated by the French National Research Agency (ANR).

REFERENCES

1. Jahng GH, Li KL, Ostergaard L, Calamante F. Perfusion magnetic resonance imaging: a comprehensive update on principles and techniques. Korean J Radiol 2014;15:554–577.
2. Willats L, Calamante F. The 39 steps: evading error and deciphering the secrets for accurate dynamic susceptibility contrast MRI. NMR Biomed 2013;26:913–931.
3. Schmid VJ, Whitcher B, Padhani AR, Taylor NJ, Yang GZ. Bayesian methods for pharmacokinetic models in dynamic contrast-enhanced magnetic resonance imaging. IEEE Trans Med Imaging 2006;25:1627–1636.
4. He L, Orten B, Do S, Karl WC, Kambadakone A, Sahani DV, Pien H. A spatio-temporal deconvolution method to improve perfusion CT quantification. IEEE Trans Med Imaging 2010;29:1182–1191.
5. Schmid VJ. Voxel-based adaptive spatio-temporal modelling of perfusion cardiovascular MRI. IEEE Trans Med Imaging 2011;30:1305–1313.
6. Frindel C, Robini MC, Rousseau D. A 3-D spatio-temporal deconvolution approach for MR perfusion in the brain. Med Image Anal 2014; 18:144–160.
7. Giacalone M, Frindel C, Robini MC, Rousseau D. Interest of non-negativity constraint in perfusion DSC-MRI deconvolution for acute stroke. In 2016 International Conference on Systems, Signals and Image Processing (IWSSIP). IEEE, Bratislava, Slovakia. 2016, pp. 89–92.
8. Østergaard L, Weisskoff RM, Chesler DA, Gyldensted C, Rosen BR. High resolution measurement of cerebral blood flow using intravascular tracer bolus passages. Part I: mathematical approach and statistical analysis. Magn Reson Med 1996;36:715–725.
9. Calamante F, Gadian DG, Connelly A. Quantification of bolus-tracking MRI: improved characterization of the tissue residue function using Tikhonov regularization. Magn Reson Med 2003;50:1237–1247.
10. Olivot JM, Mlynash M, Thijs VN, et al. Geography, structure, and evolution of diffusion and perfusion lesions in Diffusion and Perfusion Imaging Evaluation for Understanding Stroke Evolution (DEFUSE). Stroke 2009;40:3245–3251.
11. Hervé D, Mangin JF, Molko N, Bousser MG, Chabriat H. Shape and volume of lacunar infarcts: a 3D MRI study in cerebral autosomal dominant arteriopathy with subcortical infarcts and leukoencephalopathy. Stroke 2005;36:2384–2388.
12. Rivers CS, Wardlaw JM, Armitage PA, Bastin ME, Hand PJ, Dennis MS. Acute ischemic stroke lesion measurement on diffusion-weighted imaging—important considerations in designing acute stroke trials with magnetic resonance imaging. J Stroke Cerebrovasc Dis 2007;16:64–70.
13. Ogata T, Nagakane Y, Christensen S, et al. A topographic study of the evolution of the MR DWI/PWI mismatch pattern and its clinical impact—a study by the EPITHET and DEFUSE investigators. Stroke 2011;42:1596–1601.
14. Frindel C, Rouanet A, Giacalone M, et al. Validity of shape as a predictive biomarker of final infarct volume in acute ischemic stroke. Stroke 2015;46:976–981.
15. Meier P, Zierler KL. On the theory of the indicator-dilution method for measurement of blood flow and volume. J Appl Physiol 1954;6: 731–744.

16. Fieselmann A, Kowarschik M, Ganguly A, Hornegger J, Fahrig R. Deconvolution-based CT and MR brain perfusion measurement: theoretical model revisited and practical implementation details. Int J Biomed Imaging 2011;2011:14:1–14:20.
17. Giacalone M, Frindel C, Rousseau D. An unsupervised spatio-temporal regularization for perfusion MRI deconvolution in acute stroke. In 2016 European Signal Processing Conference (EUSIPCO). Budapest, Hungary, 2016, pp. 1–5.
18. Glatard T, Lartizien C, Gibaud B, et al. A virtual imaging platform for multi-modality medical image simulation. IEEE Trans Med Imaging 2013;32:110–118.
19. Kudo K, Christensen S, Sasaki M, Østergaard L, Shirato H, Ogasawara K, Wintermark M, Warach S. Accuracy and reliability assessment of CT and MR perfusion analysis software using a digital phantom. Radiology 2013;267:201–211.
20. Riordan AJ, Prokop M, Viergever MA, Dankbaar JW, Smit EJ, de Jong HW. Validation of CT brain perfusion methods using a realistic dynamic head phantom. Med Phys 2011;38:3212–3221.
21. Bosca RJ, Jackson EF. Creating an anthropomorphic digital MR phantoman extensible tool for comparing and evaluating quantitative imaging algorithms. Phys Med Biol 2016;61:974–982.
22. Mehndiratta A, Calamante F, MacIntosh BJ, Crane DE, Payne SJ, Chappell MA. Modeling the residue function in DSC-MRI simulations: analytical approximation to in vivo data. Magn Reson Med 2014;72:1486–1491.
23. Madsen MT. A simplified formulation of the gamma variate function. Phys Med Biol 1992;37:1597–1600.
24. Calamante F. Arterial input function in perfusion MRI: a comprehensive review. Prog Nucl Magn Reson Spectrosc 2013;74:1–32.
25. Calamante F, Connelly A. DSC-MRI: how accurate does the arterial input function need to be in practice? In Proceedings of the International Society for Magnetic Resonance in Medicine (ISMRM), 15th Annual Meeting. Berlin, Germany, May 19–25, 2007. p. 593.
26. Calamante F, Vonken E, van Osch MJ. Contrast agent concentration measurements affecting quantification of bolus-tracking perfusion MRI. Magn Reson Med 2007;58:544–553.
27. Jochimsen TH, Newbould RD, Skare ST, Clayton DB, Albers GW, Moseley ME, Bammer R. Identifying systematic errors in quantitative dynamic-susceptibility contrast perfusion imaging by high-resolution multi-echo parallel EPI. NMR Biomed 2007;20:429–438.
28. Meijs M, Christensen S, Lansberg MG, Albers GW, Calamante F. Analysis of perfusion MRI in stroke: to deconvolve, or not to deconvolve. Magn Reson Med 2016;76:1282–1290.
29. Smith MR, Lu H, Frayne R. Signal-to-noise ratio effects in quantitative cerebral perfusion using dynamic susceptibility contrast agents. Magn Reson Med 2003;49:122–128.
30. Sobesky J, Weber OZ, Lehnhardt FG, Hesselmann V, Neveling M, Jacobs A, Heiss WD. Does the mismatch match the penumbra? Magnetic resonance imaging and positron emission tomography in early ischemic stroke. Stroke 2005;36:980–985.
31. Takasawa M, Jones PS, Guadagno JV, et al. How reliable is perfusion MR in acute stroke? Validation and determination of the penumbra threshold against quantitative PET. Stroke 2008;39:870–877.
32. Schreiber WG, Gückel F, Stritzke P, Schmiedek P, Schwartz A, Brix G. Cerebral blood flow and cerebrovascular reserve capacity: estimation by dynamic magnetic resonance imaging. J Cereb Blood Flow Metab 1998;18:1143–1156.
33. Lin W, Celik A, Derdeyn C, An H, Lee Y, Videen T, Ostergaard L, Powers WJ. Quantitative measurements of cerebral blood flow in patients with unilateral carotid artery occlusion: a PET and MR study. J Magn Reson Imaging 2001;14:659–667.
34. Xu B, Spincemaille P, Liu T, Prince MR, Dutruel S, Gupta A, Thimmappa ND, Wang Y. Quantification of cerebral perfusion using dynamic quantitative susceptibility mapping. Magn Reson Med 2015; 73:1540–1548.
35. Wiart M, Carme S, Maï W, Larsson HB, Neyran B, Canet-Soulas E. In vivo quantification of regional myocardial blood flow: validity of the fast-exchange approximation for intravascular T_1 contrast agent and long inversion time. Magn Reson Med 2006;56:340–347.
36. Benoit-Cattin H, Collewet G, Belaroussi B, Saint-Jalmes H, Odet C. The SIMRI project: a versatile and interactive MRI simulator. J Magn Reson 2005;173:97–115.
37. Jochimsen TH, Von Mengershausen M. ODIN–object-oriented development interface for NMR. J Magn Reson 2004;170:67–78.

SUPPORTING INFORMATION

Additional Supporting Information may be found in the online version of this article.